



Highly efficient and stable Ni/CeO₂-SiO₂ catalyst for dry reforming of methane: Effect of interfacial structure of Ni/CeO₂ on SiO₂



Xiaoliang Yan^{a,*}, Tong Hu^a, Peng Liu^b, Sha Li^a, Binran Zhao^{b,*}, Qian Zhang^a, Weiyong Jiao^c, Shuai Chen^c, Pengfei Wang^c, Jingjun Lu^a, Liming Fan^a, Xiaonan Deng^a, Yun-Xiang Pan^{d,*}

^a College of Chemistry and Chemical Engineering, Taiyuan University of Technology, Taiyuan, Shanxi, 030024, PR China

^b School of Chemical Engineering, Northwest University, Xi'an, Shaanxi 710069, PR China

^c State Key Laboratory of Coal Conversion, Institute of Coal Chemistry, Chinese Academy of Sciences, 27 South Taoyuan Road, Taiyuan, 030001, PR China

^d Institute of Nano Biomedicine and Engineering, Department of Instrument Science and Engineering, School of Electronic Information and Electrical Engineering, Shanghai Jiao Tong University, Shanghai, 200240, PR China

ARTICLE INFO

Keywords:
Ni/CeO₂ catalyst
Interface
Interaction
Dry reforming
Plasma

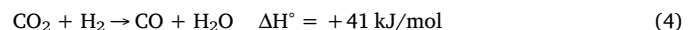
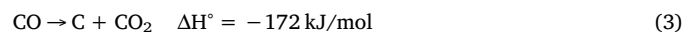
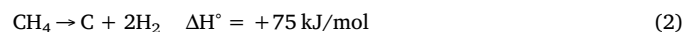
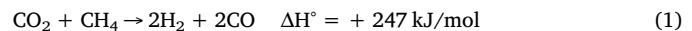
ABSTRACT

Manipulating interfacial structure and interaction between metal and supports is important for many heterogeneous catalysts with the aim at achieving high and stable activity and selectivity. In this work, two kinds of Ni/CeO₂-SiO₂ catalysts are fabricated and designed, including CeO₂ close contact with Ni nanoparticles (Ni/CeO₂-SiO₂-P) or CeO₂ away from Ni nanoparticles (Ni/CeO₂-SiO₂-C) for dry reforming of methane. Ni/CeO₂-SiO₂-P exhibits superior low-temperature activity and H₂/CO ratio compared with Ni/CeO₂-SiO₂-C. CO₂ and CH₄ conversions on the former (87.3% and 78.5%) are higher than those of the latter (80.5% and 67.8%) at 700 °C. Meanwhile, Ni/CeO₂-SiO₂-P is stable in the long-term study whereas Ni/CeO₂-SiO₂-C presents poor stability and the activity dramatically decreases in 10 h. The improved performance and stability on Ni/CeO₂-SiO₂-P originates from more reactive oxygen species and more accessible sites for the formate species on the metal-support interface. The reaction order and activation energy of both catalysts are also calculated in the kinetic studies. This work opens up new possibilities for exploring the effect of metal-support on designing highly efficient heterogeneous catalysts.

1. Introduction

Methane (CH₄) and carbon dioxide (CO₂) are not only known as greenhouse gas emissions but also regarded as main feed gases for value-added chemicals. Dry reforming of methane (DRM) is an acknowledged powerful route to convert two abundantly available greenhouse gases into the desirable syngas (CO and H₂), which is a versatile feedstock for chemical synthesis (Eq. (1)) [1–3]. Due to the fact that Ni-based catalysts possess comparable activity with noble metals, together with the abundant resource and low cost, these catalysts have been widely studied for DRM [4–8]. Nevertheless, it remains a big challenge to develop a robust catalyst that would be operated efficiently under severe reaction conditions with good stability. Ni-based catalysts deactivate quickly by coke, and suffer from sintering of Ni nanoparticles (NPs). The main origin of inactive coke deposition during DRM may occur either by CH₄ cracking (Eq. (2)) or by CO disproportionation (the Boudouard reaction, Eq. (3)). In addition, the target product H₂/CO ratio is usually less than 1 because of the side

reaction of reverse water-gas shift reaction (Eq. (4)), which leads to the considerable consumption of hydrogen along with excess of CO outlet.



Great endeavours have been made over the last decade on designing and generating anti-sintering and anti-coke Ni-based catalysts which depends on various mechanisms [9–13]. Two mechanisms for DRM reaction include monofunctional and bifunctional mechanism, where the conversion of two reactants take place on active Ni sites or on supports (for CO₂ activation) and Ni NPs (for CH₄ dissociation), respectively. Researchers have developed intriguing methodologies for designing and elucidating the structure of metal Ni and supports on the catalytic performance of DRM [14–16]. For example, Ni NPs with less

* Corresponding authors.

E-mail addresses: yanxiaoliang@tyut.edu.cn (X. Yan), zhaobr3636@126.com (B. Zhao), yxpan81@sjtu.edu.cn (Y.-X. Pan).

defect sites and more close packed planes showed a high activation energy for CH_4 dissociation, leading to an enhanced anti-coke performance on $\text{Ni}/\text{Al}_2\text{O}_3$ [14]. In addition, compared with Ni NPs (size of 17.3 nm), smaller ones, such as 2.6 nm, exhibited 4.1 times higher methane turnover frequency [15]. Furthermore, 2 nm Ni NPs on alumina prevented coke deposition and Mg-doping of alumina mitigated Ni loss into the support, thereby increasing the stability of DRM significantly [16]. Moreover, not only the structure of Ni NPs but also the supports have greatly affected the activity and stability in DRM. For example, the addition of basic promoters could enhance the activation of CO_2 , which could improve the gasification of deposited carbonaceous species, and thus contributed to the high stability of Ni catalysts [9,17]. Also, Ni catalysts with novel structures, such as core-shell, core-tube, and mesoporous framework, are beneficial to the immobilization of Ni NPs from aggregation and showed better anti-coke performance during reaction [18].

Recently, it is shown that tuning interface and intensifying interaction between Ni and supports play predominant roles in synthesizing highly efficient and stable Ni catalysts for DRM [19–21]. The more Ni-support interface contributes, the stronger reactants adsorption or/and activation on such sites compared to the bare Ni NPs [21]. Meanwhile, the stronger Ni-support interaction produces more homogeneous and smaller Ni NPs, which is in favor of high activity and stability [22,23]. Among various kinds of supports, ceria (CeO_2) has been applied as a suitable support and promoter for the catalytic reforming reaction, owing to its unique redox properties (Ce^{4+} to Ce^{3+}) and high concentration of highly reactive oxygen species. These reactive oxygen species can act as local sources or reservoirs for oxygen species, which are involved in reactions taking place on the surface of CeO_2 [24–26]. Thus, Ni- CeO_2 interface and interaction are important and essential for the anti-coke and anti-sintering performance on Ni/ CeO_2 catalysts [24]. For example, strong metal-support interaction on Ni- CeO_2 activated Ni for the dissociation of methane, as evidenced by a significant decline in the effective barrier for methane activation from 0.9 eV on Ni (111) to only 0.15 eV on $\text{Ni}/\text{CeO}_{2-x}$ (111) [25]. Furthermore, the promoting effects of Ni/ CeO_2 and Ni/YDC (yttria-doped ceria) catalysts during DRM was partly related to the availability of Ce^{3+} species within metal-support interfacial regions [26]. However, the origin of this metal-support effect on Ni/ CeO_2 catalysts for DRM reaction is not yet fully clarified.

Herein, a small portion of Ni (5 wt%) and CeO_2 (5 wt%) are loaded on inert SiO_2 to clearly clarify the effect of interface and interaction between Ni and CeO_2 for DRM performance. We applied a plasma decomposed approach for the fabrication of Ni/ CeO_2 - SiO_2 catalyst with the feature that CeO_2 is closely contacted with Ni NPs. In our previous work, plasma-decomposed Ni catalysts exhibited smaller Ni particles size, less defect sites, and stronger Ni-support interaction than those of thermal decomposed ones. It still remains sophisticated to disclose the main origin for better anti-coke and anti-sintering performances because complex factors are affecting the activity and stability [27,28]. In this work, the only difference is between Ni metal and CeO_2 support, which can be successfully used to clarify the mechanism of highly efficient and stable Ni/ CeO_2 - SiO_2 for DRM. In addition, X-ray diffraction (XRD), hydrogen temperature programmed reduction (H_2 -TPR), X-ray photoelectron spectroscopy (XPS), transmission electron microscopy (TEM), scanning transmission electron microscopy-energy-dispersive X-ray spectroscopy (STEM-EDX), CO pulse chemisorption, thermogravimetric-mass spectrometric (TG-MS), and diffuse reflectance infrared Fourier transform spectroscopy (DRIFTS) measurements are applied to study the structure of the catalyst and to further unravel the structure-performance relationship.

2. Experimental

2.1. Catalyst synthesis

The inert silica powder support (Sigma-Aldrich) was firstly calcined in air at 500 °C for 4 h. Afterwards nickel nitrate and cerium nitrate (Tianjin Kemiou Chemical Reagent Co., Ltd., China) aqueous solution was co-impregnated into the SiO_2 by the incipient wetness impregnation method and then placed at the room temperature for 12 h. The sample was dried at 110 °C for 12 h. Afterwards, highly energetic electrons and oxygen atoms generated by dielectric-barrier discharge plasma with following calcination (500 °C for 3 h in air) are employed to fabricate Ni catalyst. The details of the decomposition process have been previously reported [27,28]. The catalyst is named as NiO/CeO_2 - SiO_2 -P. In addition, the dried sample was directly treated at 500 °C for 3 h in air, and the catalyst is named as NiO/CeO_2 - SiO_2 -C. ICP-AES results demonstrated that Ni and Ce loadings are the same as 5.0 and 4.1 wt% for NiO/CeO_2 - SiO_2 -P and NiO/CeO_2 - SiO_2 -C, separately.

The original impregnated sample exhibits light green color (Fig. S1a). After the plasma decomposition, the color of the sample changes to light gray, indicating effective decomposition of the nitrite precursors of nickel and cerium. In our previous work, we have discovered that highly energetic electrons and ozone play vital roles in the decomposition of the precursors, contributing to a thermally controllable way under the treatment temperature below 200 °C [27,28]. Moreover, thermal calcination is further applied to make sure complete decomposition of the precursors. Notably, with a low Ni loading content and appropriate calcination temperature, NiO particle size and its distribution on both NiO/CeO_2 - SiO_2 -C and NiO/CeO_2 - SiO_2 -P samples are almost the same as illustrated by the TEM images in Fig. S1b and c.

2.2. Characterizations

An inductively coupled-plasma atomic emission spectroscopy (Thermo iCAP 6300 spectrometer) was employed to measure the nickel and cerium contents on NiO/CeO_2 - SiO_2 . Powder XRD patterns of the samples were measured from 10 to 90° by step scanning on a Rigaku D/Max-2500 diffractometer. TEM and STEM-EDX analyses were performed on a FEI Tecnai G²-F20 system operated at 200 kV. A Thermo SCIENTIFIC ESCALAB 250XI spectrometer was applied to conduct X-ray photoelectron spectroscopy tests. The binding energies were calibrated with C1 s peak at 284.8 eV. The deposited carbon on the used catalysts was analyzed by oxidation in air and the produced CO_2 was monitored by a Setaram SETSYS TGA thermoanalyzer (TG) coupled with Hiden HPR20 QIC R&D mass spectrometer (MS).

A Micromeritics AutoChem II 2920 instrument was applied to analyze the H_2 -TPR. 0.1 g sample was pretreated in 30 mL min⁻¹ of He for 1 h at 300 °C. Afterwards the system was cooled to 50 °C, followed by heating to 600 °C with a rate of 10 °C min⁻¹ in 10% H_2 /He (30 mL min⁻¹) and signal of the thermal conductivity detector (TCD) was recorded. The same apparatus was applied to perform CO pulse chemisorption. The sample was first reduced at 500 °C for 2 h in 10% H_2 /He (30 mL min⁻¹), followed by cooling down to 0 °C in He (30 mL min⁻¹) to avoid the formation of $\text{Ni}(\text{CO})_4$ species, and then 5 mL of 5% CO/He was injected into the reduced sample at 5 min intervals according to the pulse method until saturation adsorption was observed.

DRIFTS was applied to elucidate the reaction mechanism of the samples in DRM. The DRIFTS spectra were collected on a FTIR spectrometer (Bruker Vertex 70) equipped with a liquid nitrogen cooled Mercury-Cadmium-Tellurium (MCT) detector and a diffuse reflectance accessory (Praying Mantis, Harrick). The samples were firstly reduced in a tube furnace at 500 °C for 2 h in H_2 . Afterwards, ~35 mg of sample was placed into the cup of a reaction chamber (HVC, Harrick) and sealed with ZnSe windows, and then reduced in 5% H_2 (30 mL min⁻¹) at 300 °C for 1 h, and followed by purging in He (30 mL min⁻¹) for

30 min, and then the temperature was then increased to 400 °C in the same condition. Background spectrum was recorded under He condition. After that, 5% CO₂/He (10 mL min⁻¹) and 5% CH₄/He (10 mL min⁻¹) were introduced into the cell for 30 min. Background spectrum subtracted at a resolution of 4 cm⁻¹ and 128 scans was recorded as the spectrum.

2.3. Catalytic performance

Dry reforming of CH₄ was carried out on a fixed-bed quartz tube reactor (6 mm of inner diameter). The powder sample was pelletized and crushed into 40–60 mesh. 50 mg of catalysts was firstly blended with 500 mg of silica sand (similar size with catalyst) and then packed in the reactor between the two parts of quartz wool. Then, the catalyst was heated up to 500 °C in Ar (50 mL min⁻¹) at a constant heating rate of 10 °C min⁻¹. Afterwards, the catalyst was reduced in H₂ (50 mL min⁻¹) for 2 h. After the reduction, the catalyst was purged in Ar (50 mL min⁻¹) for 1 h and heated up to the reaction temperature. At last, CH₄/CO₂/Ar with a molar ratio of 1:1:2 was fed into the reactor for dry reforming of CH₄. The gas hour space velocity was controlled at 4.8 × 10⁴ mL g⁻¹ h⁻¹. The outlet gas was analyzed by a thermal conductivity detector (TCD) with a TDX-01 column (3 m) on a gas chromatograph (GC, SP-3420 A). An ice trap was used to get rid of water to protect the GC. The catalytic performance was tested at the reaction temperature of 600, 700, and 800 °C. To further study the stability of the catalyst, the temperature was maintained at 700 °C. CH₄ (X_{CH4}) and CO₂ (X_{CO2}) conversion was measured using the following equations:

$$X_{\text{CH}_4} (\%) = (F_{\text{CH}_4,\text{in}} - F_{\text{CH}_4,\text{out}}) / F_{\text{CH}_4,\text{in}} \times 100 \quad (5)$$

$$X_{\text{CO}_2} (\%) = (F_{\text{CO}_2,\text{in}} - F_{\text{CO}_2,\text{out}}) / F_{\text{CO}_2,\text{in}} \times 100 \quad (6)$$

where F_{CH₄,in}, F_{CH₄,out}, F_{CO₂,in}, and F_{CO₂,out} are the inlet and outlet flows of methane and CO₂, respectively.

3. Results

3.1. Catalysts characterizations

The structural properties of NiO/CeO₂-SiO₂ samples were studied by XRD and the corresponding patterns are shown in Fig. 1. With the

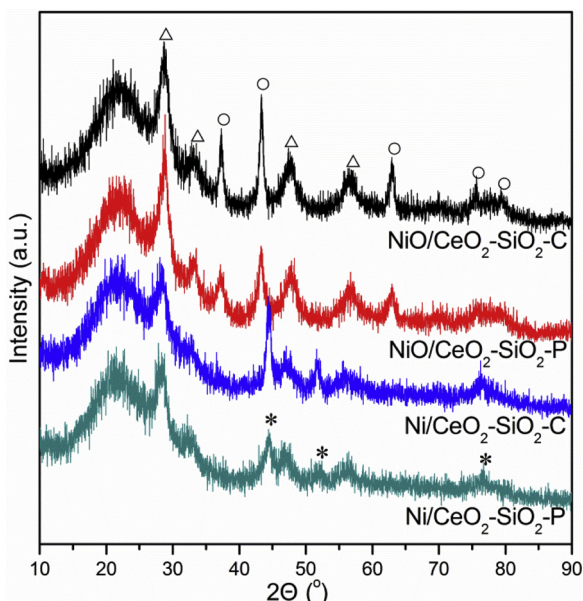


Fig. 1. XRD patterns of NiO/CeO₂-SiO₂-C, NiO/CeO₂-SiO₂-P, Ni/CeO₂-SiO₂-C, and Ni/CeO₂-SiO₂-P. Empty triangle represents CeO₂, empty circle refers to NiO, and star represents Ni.

Table 1

The results of Ni dispersion, Ni surface area, and particle size of Ni/CeO₂-SiO₂-C and Ni/CeO₂-SiO₂-P obtained from CO chemisorption.

Catalysts	D (%)	S _{Ni} (m ² /g)	d (nm)
Ni/CeO ₂ -SiO ₂ -C	10.9	72.9	9.2
Ni/CeO ₂ -SiO ₂ -P	12.1	80.7	8.3

presence of amorphous SiO₂, one broad peak is shown at 22.1° for both samples, and four diffraction peaks (empty black triangle) at around 20 of 28.7°, 33.5°, 47.4°, and 56.8° are also presented, which corresponds to the (111), (200), (220), and (311) planes for CeO₂ (PDF No. 81-0792), respectively. In addition, five diffraction peaks (empty black circle) appear on the samples at 37.2°, 43.3°, 62.9°, 75.4°, and 79.4°, matching well with the (111), (200), (220), (311), and (222) planes for NiO (PDF No. 47-1049), respectively. Notably, hardly detected distinct difference between two patterns was observed, suggesting the similar crystalline and particle size of NiO and CeO₂. Furthermore, three main peaks (star marks) are clearly observed on Ni/CeO₂-SiO₂ at 44.5°, 51.7°, and 76.5°, which correspond to the (111), (200), and (220) planes for Ni (PDF No. 04-0850) after H₂ reduction at 500 °C. There is no considerable structural change of CeO₂ and SiO₂ after the reduction. Based on CO chemisorption as shown in Table 1, Ni/CeO₂-SiO₂ catalysts possess similar particle size of less than 10 nm: 9.2 nm for Ni/CeO₂-SiO₂-C and 8.3 nm for Ni/CeO₂-SiO₂-P, separately. The result demonstrated that the particle size of Ni NPs over Ni/CeO₂-SiO₂-C and Ni/CeO₂-SiO₂-P are well controlled to less than 10 nm with small Ni loading content and appropriate reduction temperature.

H₂-TPR was further applied to investigate the reducibility of NiO/CeO₂-SiO₂. Fig. S2 shows the results of the H₂-TPR for NiO/CeO₂-SiO₂-C and NiO/CeO₂-SiO₂-P. On the H₂-TPR profiles, the reduction profiles were deconvoluted into two peaks, one low temperature (LT) peak at ~300 °C and one high temperature (HT) peak at ~380 °C. The former is attributed to the reduction of surface ceria species and small NiO NPs; whereas the latter is indicative of an intimate contact between nickel and ceria enhancing the oxygen mobility [29,30]. The ratio of HT to LT peak is 35.3% and 56.8% on NiO/CeO₂-SiO₂-C and NiO/CeO₂-SiO₂-P, respectively. This reveals a closer interaction between Ni NPs and CeO₂ on NiO/CeO₂-SiO₂-P.

Surface structures of NiO/CeO₂-SiO₂-C and NiO/CeO₂-SiO₂-P were also studied by XPS methods. Both samples exhibit a primary Ni 2p_{3/2} peak at 856.7 eV and a small satellite peak (Fig. S3), because of the decomposition of Ni precursor to nickel oxide species [31]. XPS spectra of Ce 3d regions could be deconvoluted into ten peaks, as shown in Fig. 2a and b. The peaks of v, v'', v''', u, u'', and u''' correspond to the presence of Ce⁴⁺ species, and the peaks of v°, v''', u°, and u''' originate from the contribution of Ce³⁺ species [32–35]. This reveals that both NiO/CeO₂-SiO₂-C and NiO/CeO₂-SiO₂-P contain Ce³⁺ and Ce⁴⁺ species. The formation and stabilization of Ce³⁺ ions contribute to the spontaneous presence of reactive oxygen species in the CeO₂ lattice on the interface of the Ni NPs and CeO₂ oxide. Based on the peaks area of Ce³⁺ species to the total Ce³⁺ and Ce⁴⁺ species, the relative content of Ce³⁺ is 0.18 and 0.24 for NiO/CeO₂-SiO₂-C and NiO/CeO₂-SiO₂-P, respectively (Table 2). In addition, the ratio of Ce/Ni of NiO/CeO₂-SiO₂-P (1.14) is higher than that of NiO/CeO₂-SiO₂-C (0.16). Therefore, more CeO₂ with reactive oxygen species covers NiO on plasma generated NiO/CeO₂-SiO₂-P. O 1 s XPS spectra of NiO/CeO₂-SiO₂-C and NiO/CeO₂-SiO₂-P are shown in Fig. 2c. There are two types of oxygen species formed on the samples, and can be classified as O_α and O_β species. These O_α species could be assigned to oxygen ions (O²⁻, O₂²⁻, and O-) and the O_β species refer to surface hydroxyl groups or the adsorbed oxygen, respectively [35,36]. Based on the area integrals, the ratio of O_α (oxygen ions) to O_β (surface hydroxyl groups) is calculated. The ratio of NiO/CeO₂-SiO₂-P (43.7%) is higher than that of NiO/CeO₂-SiO₂-C (30.2%), indicating the increasing number of active oxygen

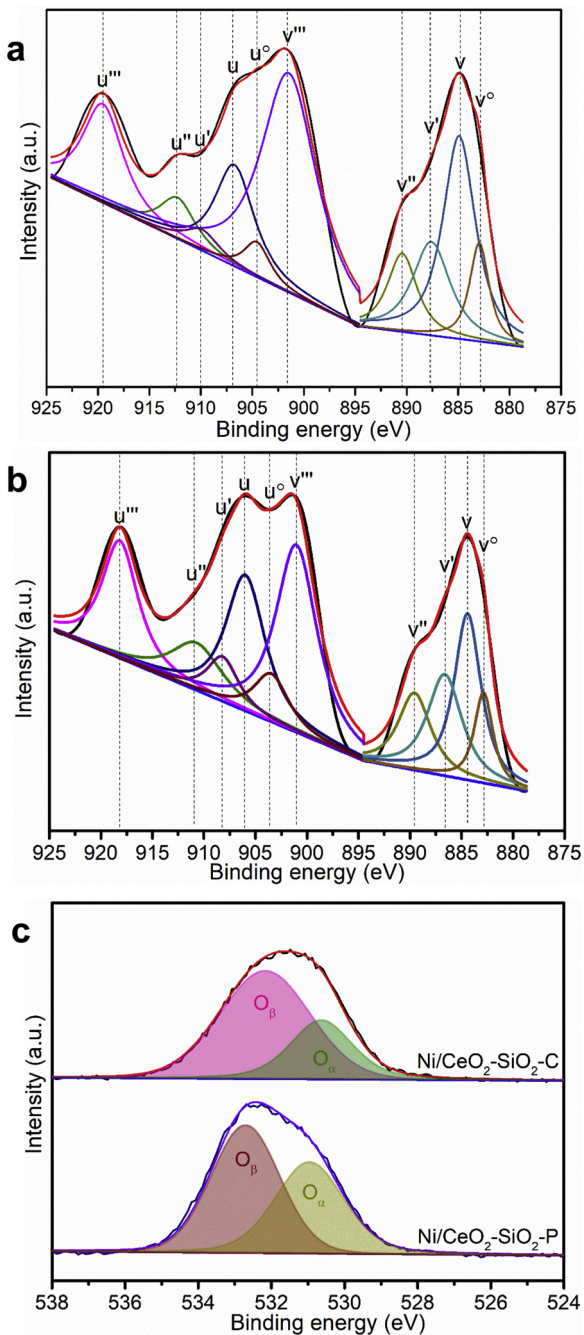


Fig. 2. High resolution XPS spectra of Ce 3d of (a) NiO/CeO₂-SiO₂-C and (b) Ni/CeO₂-SiO₂-P and (c) XPS spectra of O 1s of the two samples.

Table 2
XPS derived atomic ratio of NiO/CeO₂-SiO₂-C and NiO/CeO₂-SiO₂-P.

Catalysts	C (%)	Ni (%)	Ce (%)	O (%)	Si (%)	Ce/Ni	Ce ³⁺ /Ce _{tot}
NiO/CeO ₂ -SiO ₂ -C	56.91	0.94	0.15	25.05	16.96	0.16	0.18
NiO/CeO ₂ -SiO ₂ -P	54.63	0.29	0.33	27.51	17.24	1.14	0.24

species on NiO/CeO₂-SiO₂-P.

3.2. Structural study of Ni/CeO₂-SiO₂ catalysts

The morphological and structural properties of Ni/CeO₂-SiO₂

catalysts after H₂ reduction are further investigated by TEM measurements as shown in Fig. 3. Obviously, black particles are highly dispersed on amorphous SiO₂ and no aggregation of large particle is detected on both Ni/CeO₂-SiO₂-C (Fig. 3a and b) and Ni/CeO₂-SiO₂-P (Fig. 3d and e) with H₂ reduction at 500 °C. We further used STEM/EDS mapping to illustrate the fine structure of Ni/CeO₂-SiO₂-C and Ni/CeO₂-SiO₂-P in Fig. 3g and h. The elemental distributions of nickel element in Ni/CeO₂-SiO₂-C and Ni/CeO₂-SiO₂-P are distributed separately. Notably, the elemental distributions of cerium element in both catalysts differ greatly. Cerium element (green) in Ni/CeO₂-SiO₂-C scatters and forms less interfacial sites with nickel element; whereas more Ni-support interfacial sites are generated on Ni/CeO₂-SiO₂-P as evidenced by the fact that plentiful cerium element (red) occupied the vacancy of nickel element. This result is well consistent with the observation of high resolution TEM analyses in Fig. 3c and f. For Ni/CeO₂-SiO₂-C, the lattice spacing, 0.204 nm for Ni and 0.312 nm for CeO₂ particle, correspond well with the characteristic of Ni (111) and CeO₂ (111) planes, respectively (Fig. 3c). It can also be clearly observed that Ni and CeO₂ locate on SiO₂ separately. However, in the case of Ni/CeO₂-SiO₂-P, in addition to Ni (111) plane, the lattice spacing of 0.27 nm agrees with the (200) plane of CeO₂ (Fig. 3f). Ni and CeO₂ are in close contact with each other, contributing to the formation of more Ni-support interface.

To dig deeper into the structure of Ni/CeO₂-SiO₂ and to gain some more interface insights, we conducted XPS to analyze the reduced Ni catalysts (Fig. S4). According to the deconvoluted results, the reduced Ni/CeO₂-SiO₂ possesses both Ce³⁺ and Ce⁴⁺ species. Based on the peaks area of Ce³⁺ species to the total Ce³⁺ and Ce⁴⁺ species, the relative content of Ce³⁺ is 0.33 and 0.41 for Ni/CeO₂-SiO₂-C and Ni/CeO₂-SiO₂-P, respectively. In Ni 2p_{3/2} region, besides the presence of Ni²⁺ species (due to the easily oxidation of metallic Ni), both catalysts exhibit the peaks, characterized for the formation of Ni⁰ species. The binding energy of Ni⁰ species on Ni/CeO₂-SiO₂-P shifts to lower value than that of Ni/CeO₂-SiO₂-C. This is originated from the generation of more close interaction between Ni and Ce³⁺ species on Ni/CeO₂-SiO₂-P, owing to the fact that Ce³⁺ species provide more electrons to Ni⁰ species.

3.3. Catalytic investigation of dry reforming of methane

The catalytic behaviors of Ni/CeO₂-SiO₂-C and Ni/CeO₂-SiO₂-P for the DRM were studied at the temperature of 600, 700, and 800 °C. The evolution of CH₄ and CO₂ conversions and H₂/CO ratio can be illustrated as a function of reaction temperature (Table 3). The conversions of both CH₄ and CO₂ over the Ni/CeO₂-SiO₂-P are higher than that over Ni/CeO₂-SiO₂-C at 600 and 700 °C. For example, at 700 °C, the conversions of CH₄ and CO₂ are 87.3% and 78.5% for the former, whereas the conversions are only 80.5% and 67.8% for the latter. At 800 °C, both conversions of CH₄ and CO₂ are comparable for the catalysts. This is well matched with our previous study that plasma-generated Ni-based catalysts possessed a better low temperature catalytic performance than the thermal ones [28]. Generally, reverse water gas shift reaction (RWGS) can lead to higher conversion of CO₂, compared with that of CH₄. The H₂/CO ratio is also higher for the Ni/CeO₂-SiO₂-P in comparison with that of Ni/CeO₂-SiO₂-C at 600 and 700 °C, as the RWGS reaction becomes less favored. Besides, this ratio is similar on the two catalysts at 800 °C.

3.4. Stability of dry reforming of CH₄

The long-term stability of Ni/CeO₂-SiO₂-C and Ni/CeO₂-SiO₂-P was investigated for dry reforming of CH₄ at 700 °C. As shown in Fig. 4a, CO₂ and CH₄ conversions on conventional Ni/CeO₂-SiO₂-C at 700 °C decline significantly even at the first 10 h. CO and CH₄ conversions decrease from about 84% to 73% and from 71% to 58%, separately within 15 h. Distinctly different from Ni/CeO₂-SiO₂-P, both CO₂ and CH₄ conversions of Ni/CeO₂-SiO₂-P exhibit stable values of 88% and

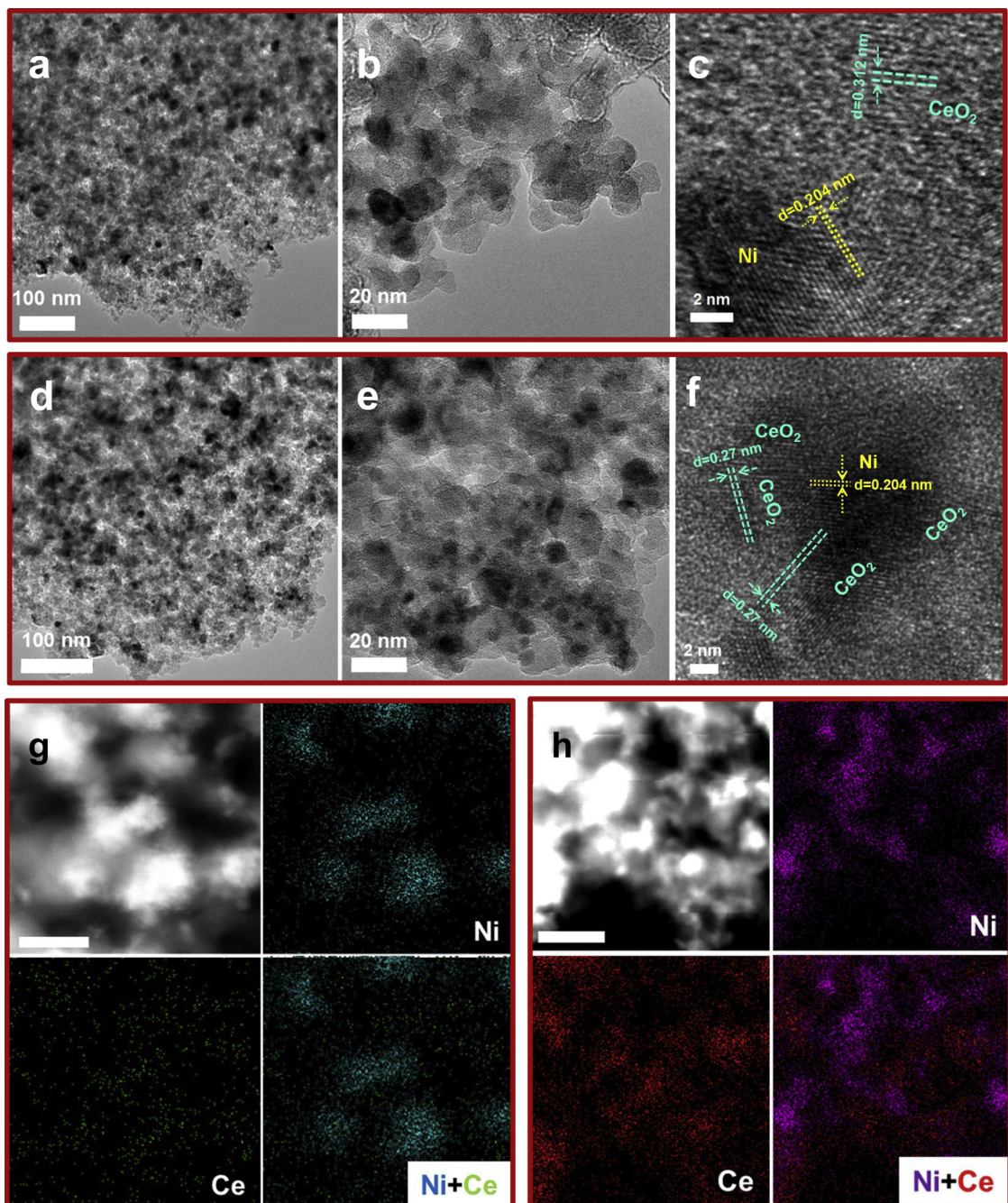


Fig. 3. TEM images of (a, b, c) Ni/CeO₂-SiO₂-C and (d, e, f) Ni/CeO₂-SiO₂-P. STEM/EDS mapping of (g) Ni/CeO₂-SiO₂-C and (h) Ni/CeO₂-SiO₂-P. The scale bar is 50 nm.

Table 3

Conversions of CO₂ and CH₄ as well as H₂/CO ratio for Ni/CeO₂-SiO₂-C and Ni/CeO₂-SiO₂-P at 600, 700, and 800 °C for 1 h.

Temperature (°C)	Ni/CeO ₂ -SiO ₂ -C			Ni/CeO ₂ -SiO ₂ -P		
	X _{CO2} (%)	X _{CH4} (%)	H ₂ /CO	X _{CO2} (%)	X _{CH4} (%)	H ₂ /CO
600	66.5	51.4	0.77	72.8	59.2	0.83
700	80.5	67.8	0.85	87.3	78.5	0.89
800	97.2	92.1	0.92	97.5	92.4	0.94

78% under the same catalytic condition, respectively, without any obvious change in the 50 h. The time dependent H₂ to CO ratio of the Ni/CeO₂-SiO₂ catalysts are given in Fig. 4b. The ratio of H₂/CO on Ni/CeO₂-SiO₂-C and

CeO₂-SiO₂-P remains stable at ~0.88 in 50 h and is higher than that on Ni/CeO₂-SiO₂-C in 10 h, which decreases from 0.87 to 0.83. A high H₂/CO ratio reveals that the catalyst inhibits the RWGS reaction on Ni/CeO₂-SiO₂-P. Therefore Ni/CeO₂-SiO₂-P exhibits better stability in dry reforming of CH₄ than that of Ni/CeO₂-SiO₂-C.

3.5. Characterization of the used Ni/CeO₂-SiO₂ catalysts

Generally, based on the oxidation temperature, including highly reactive carbon adatom active carbon (C_α), less active carbonaceous species (C_β), and inactive graphitic carbon (C_γ), the carbon deposition on Ni-based catalysts is classified into three forms [37–40]. We analyzed carbon species formed after stability test on Ni/CeO₂-SiO₂-C and Ni/CeO₂-SiO₂-P by applying O₂-TPO experiments (Fig. 5). Peaks at 107,

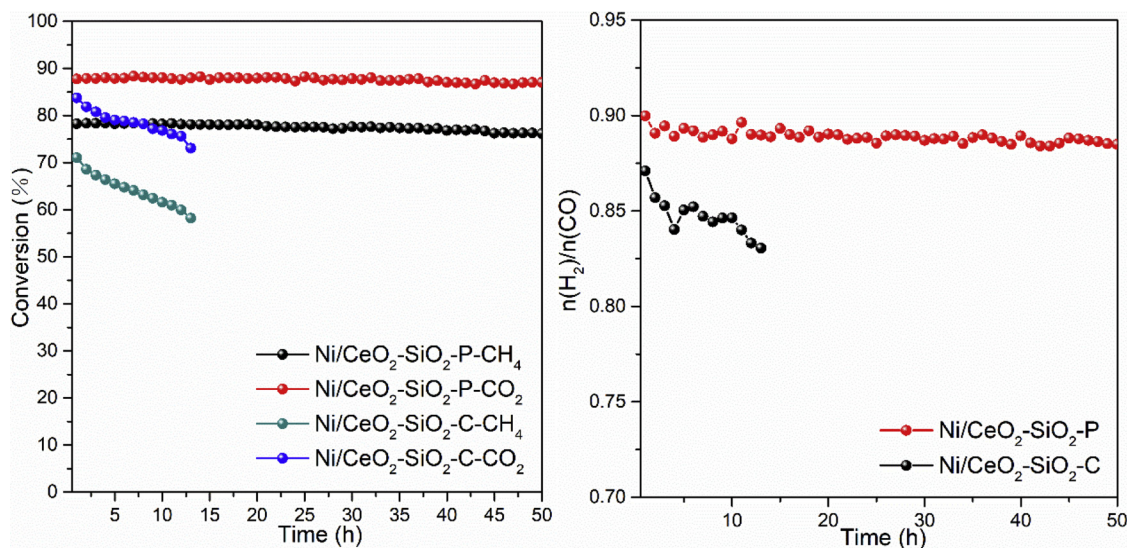


Fig. 4. Stability test of $\text{Ni}/\text{CeO}_2\text{-SiO}_2\text{-C}$ and $\text{Ni}/\text{CeO}_2\text{-SiO}_2\text{-P}$ at $700\text{ }^\circ\text{C}$.

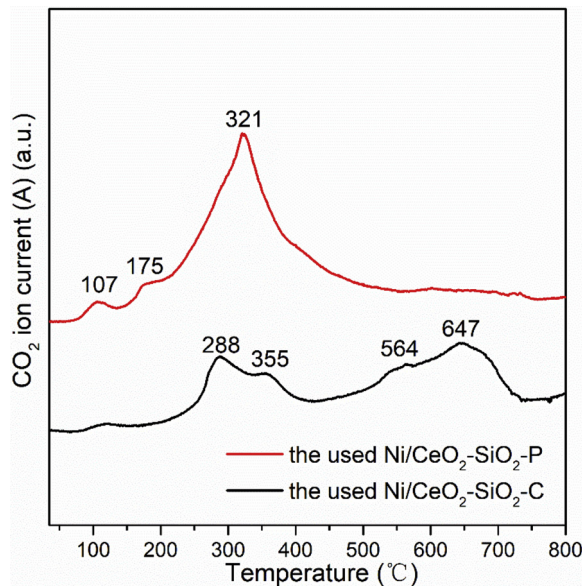


Fig. 5. $\text{O}_2\text{-TPO}$ of the used $\text{Ni}/\text{CeO}_2\text{-SiO}_2\text{-C}$ and $\text{Ni}/\text{CeO}_2\text{-SiO}_2\text{-P}$.

175, and $321\text{ }^\circ\text{C}$ appear on the $\text{O}_2\text{-TPO}$ curve of $\text{Ni}/\text{CeO}_2\text{-SiO}_2\text{-P}$. All of these peaks originate from the oxidation of active C_{α} species, which is mainly caused by the presence of amorphous carbon. In addition, no peak is shown when the temperature is higher than $400\text{ }^\circ\text{C}$. This suggests that the formation of less and inactive carbon is efficiently suppressed on $\text{Ni}/\text{CeO}_2\text{-SiO}_2\text{-P}$. However, regarding the $\text{O}_2\text{-TPO}$ curve of $\text{Ni}/\text{CeO}_2\text{-SiO}_2\text{-C}$, in addition to the low temperature peaks at 288 and $355\text{ }^\circ\text{C}$, there are two peaks located at 564 and $647\text{ }^\circ\text{C}$. The former peak belongs to the oxidation of less active C_{β} species, and the latter peak corresponds to the generation of inactive C_{γ} species, leading to serious deactivation of the catalytic performance.

In order to check the morphology of the deposited carbon species, TEM measurements were further carried out. TEM images of the used $\text{Ni}/\text{CeO}_2\text{-SiO}_2\text{-C}$ and $\text{Ni}/\text{CeO}_2\text{-SiO}_2\text{-P}$ are shown in Fig. 6. Clearly, large amounts of carbon filaments (like CNTs) exist on the used $\text{Ni}/\text{CeO}_2\text{-SiO}_2\text{-C}$ as some of Ni NPs are inside or on the top of the filaments. In addition, Ni NPs encapsulated in carbon onions can also be observed with white circle in Fig. 6a. Moreover, the presence of graphitic carbon in the used $\text{Ni}/\text{CeO}_2\text{-SiO}_2\text{-P}$ is not detected through careful observation (Fig. 6c and d), and the type of carbon is not confirmed because of

amorphous nature of the deposited carbon.

4. Discussions

4.1. Mechanism study of $\text{Ni}/\text{CeO}_2\text{-SiO}_2$ catalysts for dry reforming of CH_4

Since the particle size and its distribution of Ni NPs on $\text{Ni}/\text{CeO}_2\text{-SiO}_2\text{-C}$ and $\text{Ni}/\text{CeO}_2\text{-SiO}_2\text{-P}$ are nearly the same, thus, in the preceding sections of this work it is safe to study the effect of interface between Ni and CeO_2 on inert SiO_2 support for the catalytic performance of dry reforming of CH_4 . The main feature of $\text{Ni}/\text{CeO}_2\text{-SiO}_2\text{-P}$ is in close interaction between Ni NPs and CeO_2 on SiO_2 , contributing to more metal-support interface (Fig. 3). Ni NPs are away from CeO_2 on SiO_2 for $\text{Ni}/\text{CeO}_2\text{-SiO}_2\text{-C}$. Compared with $\text{Ni}/\text{CeO}_2\text{-SiO}_2\text{-C}$, $\text{Ni}/\text{CeO}_2\text{-SiO}_2\text{-P}$ has more reactive oxygen species in the CeO_2 lattice on the Ni- CeO_2 interface (Fig. 2).

In order to clarify the reaction mechanism, *in situ* DRIFTS analysis was applied to get deeper into the intermediate species during the reaction. Fig. 7 shows the DRIFTS spectra for $\text{Ni}/\text{CeO}_2\text{-SiO}_2\text{-C}$ and $\text{Ni}/\text{CeO}_2\text{-SiO}_2\text{-P}$ under dry reforming of methane condition at $400\text{ }^\circ\text{C}$ for different reaction time. The DRIFTS spectra of $\text{Ni}/\text{CeO}_2\text{-SiO}_2\text{-C}$ show eight bands at $3016, 2300\text{--}2400, 2098, 1942, 1776, 1540, 1255$, and 1114 cm^{-1} , respectively. The band at 3016 cm^{-1} can be assigned to CH_4 , which then dissociates into CH_x species. The band at $2300\text{--}2400\text{ cm}^{-1}$ refers to the appearance of CO_2 in gas phase. The bands at 2098 and 1942 cm^{-1} correspond to the presence of linearly adsorbed and bridge adsorbed CO , respectively. The bands at $1776, 1540$, and 1255 cm^{-1} are characterized for the formation of carbonate species (CO_3^{2-}) [41]. The band at 1114 cm^{-1} is attributed to the presence of negatively charged CO_2^- species [42]. Whereas the DRIFTS spectra of $\text{Ni}/\text{CeO}_2\text{-SiO}_2\text{-P}$ exhibit a new band at 1398 cm^{-1} , owing to the presence of formate species (HCOO^-), except for the afore-mentioned ones [43].

It has been widely accepted that dry reforming of methane on Ni catalysts follows the bifunctional mechanism, that is, CH_4 and CO_2 are activated on Ni NPs and support, separately [44,45]. For $\text{Ni}/\text{CeO}_2\text{-SiO}_2\text{-C}$, Ni and CeO_2 locate on SiO_2 separately, leading to the untimely reaction of the activated species on Ni NPs and CeO_2 . However, the close interaction and interface between Ni and CeO_2 on $\text{Ni}/\text{CeO}_2\text{-SiO}_2\text{-P}$ promote the reaction of CO_2^- with H on Ni NPs from CH_4 dissociation to form HCOO^- . The results are well matched with the findings reported that the interfacial metal-support centers promoted the surface formate in dry reforming of methane [45,46]. Thus, more

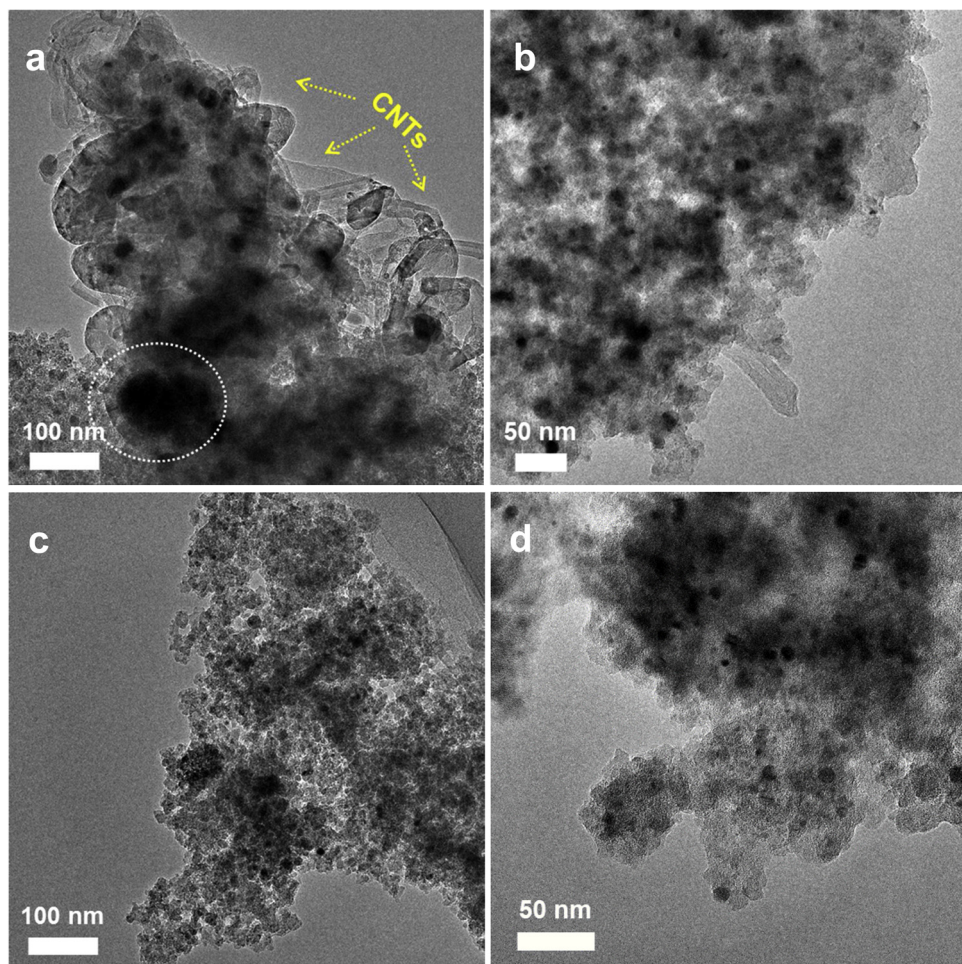


Fig. 6. TEM images of the used (a, b) Ni/CeO₂-SiO₂-C and (c, d) Ni/CeO₂-SiO₂-P.

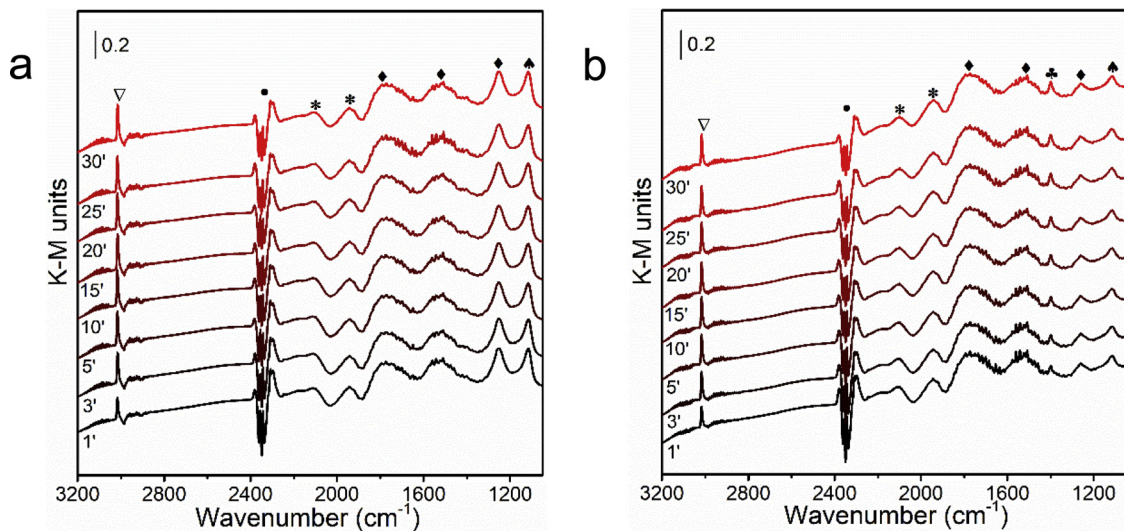


Fig. 7. DRIFTS of CH₄ + CO₂ reaction on (a) Ni/CeO₂-SiO₂-C and (b) Ni/CeO₂-SiO₂-P at 400 °C. Reaction time at 1, 3, 5, 10, 15, 20, 25, and 30 min. ▽: CH₄, ●: CO₂, ◆: CO₃²⁻, *: CO, ▲: HCOO⁻; ♦: CO₂⁻.

metal-support interface on Ni/CeO₂-SiO₂-P facilitates the synchronous activation of CH₄ and CO₂ to produce HCOO⁻ as an intermediate, contributing to a better catalytic performance than that of Ni/CeO₂-SiO₂-C.

4.2. Kinetic study of Ni/CeO₂-SiO₂ catalysts for dry reforming of CH₄

We further conduct the kinetic study of Ni/CeO₂-SiO₂-C and Ni/CeO₂-SiO₂-P for DRM reaction. Firstly, the effects of external and internal diffusion limitation are ruled out by varying the weight hourly space velocity with a fixed catalyst mass and by using catalyst with

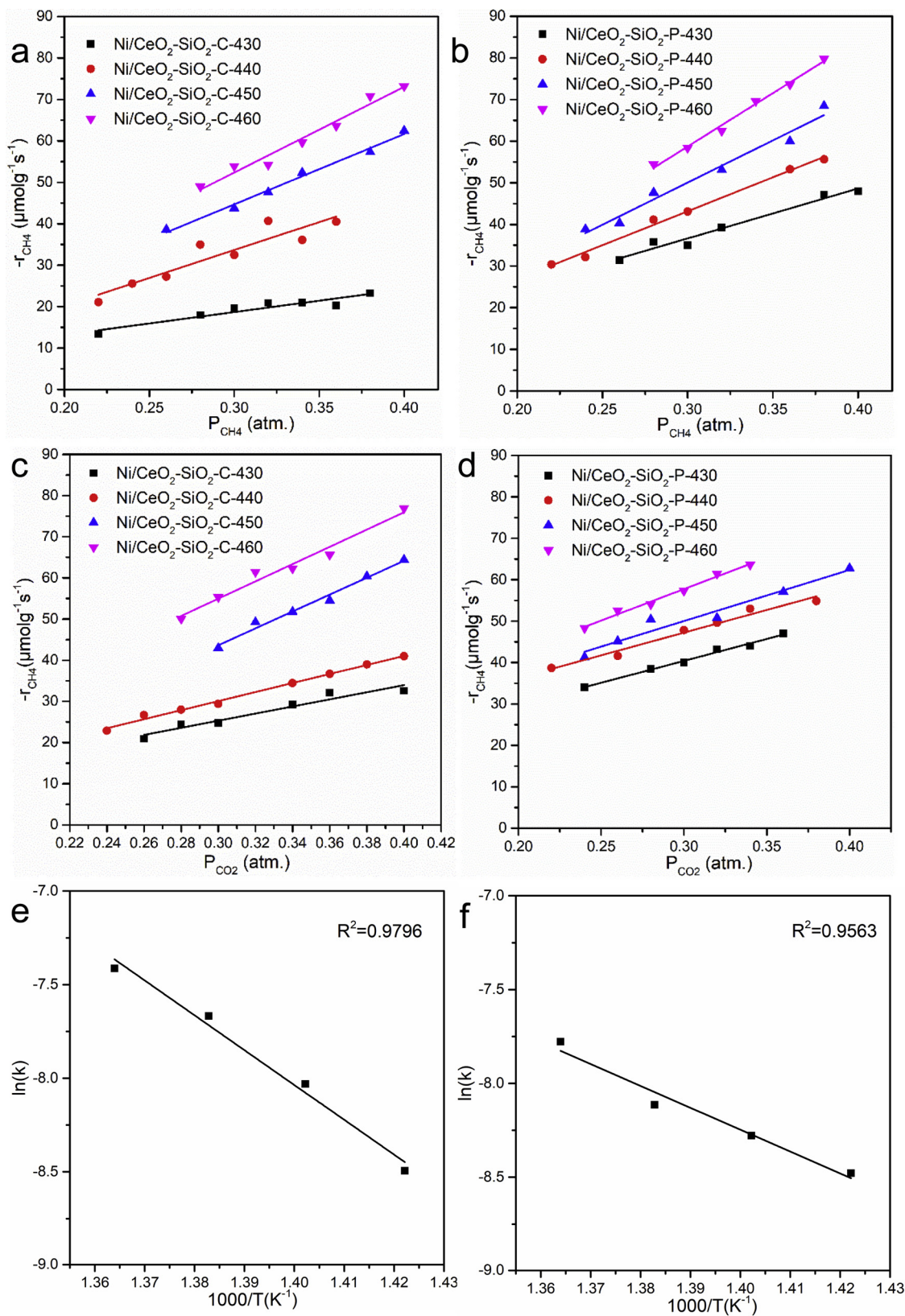


Fig. 8. Changes of reaction rates as the partial pressure of reactants changes and the corresponding Arrhenius plots for CH₄ activation energies over Ni/CeO₂-SiO₂-C (a, c, e) and Ni/CeO₂-SiO₂-P (b, d, f).

different diameters, respectively (Fig. S5). The unchangeable activity with changing the mass or diameter of the catalysts reveals that the DRM reaction is in the kinetic region. Then, the influences of mass transport limitation and heat transfer are removed by checking the

Weisz-Prater criterion (Eq. (7)) and the Mears criterion (Eq. (8)), respectively. The calculations in detail are shown in the supporting information. The values of C_{WP} in Eq. (7) are 2.16×10^{-1} and 2.42×10^{-1} for Ni/CeO₂-SiO₂-C and Ni/CeO₂-SiO₂-P, respectively,

Table 4

Kinetic parameters of Ni/CeO₂-SiO₂-C and Ni/CeO₂-SiO₂-P in dry reforming of CH₄.

Temperature (°C)	Ni/CeO ₂ -SiO ₂ -C			Ni/CeO ₂ -SiO ₂ -P		
	k	a	b	k	a	b
430	2.05×10^{-2}	1.01	0.82	2.08×10^{-2}	0.86	0.67
440	3.25×10^{-2}	1.10	1.03	2.42×10^{-2}	0.86	0.69
450	4.68×10^{-2}	1.12	1.08	2.90×10^{-2}	0.92	0.73
460	6.03×10^{-2}	1.20	1.09	4.19×10^{-2}	0.95	0.93

both of which are less than 1, indicating no internal diffusion limitations exist. The values of the Mears criterion in Eq. (8) are 3.42×10^{-4} and 3.82×10^{-4} for Ni/CeO₂-SiO₂-C and Ni/CeO₂-SiO₂-P, respectively, which are both less than 3, suggesting that interphase or intraparticle heat transfer or mass transport limitations have been eliminated.

$$C_{WP} = \frac{-r'_A(\text{obs})\rho_c R^2}{D_e C_{As}} < 1 \quad (7)$$

$$\frac{-r'_A R^2}{C_{Ab} D_e} < \frac{1 + 0.33\gamma_b}{|n - \gamma_b \beta_b|(1 + 0.33n\omega)} \quad (8)$$

The kinetic experiments are carried out on Ni/CeO₂-SiO₂ catalysts by changing the partial pressure of one reactant, while remaining the partial pressure of the other reactant constant in a differential tubular reactor. The reaction temperature ranges from 430 to 460 °C to ensure that CH₄ conversion is below 10%. The reaction rate is calculated by differential method shown in Eq. (9).

$$-r_i = dX_i/d(W_{\text{cat}}/F_i) \quad (9)$$

where r_i, X_i, and F_i refer to the reaction rate, the conversion, and the flow of component i, respectively, and W_{cat} corresponds to the weight of catalyst. In addition, reaction rate r_i can also be considered as a function of partial pressures of the reactants. For DRM, it can be expressed as follows:

$$r_{\text{CH}_4} = k(p_{\text{CH}_4})^a \cdot (p_{\text{CO}_2})^b \quad (10)$$

where k, a, b are the unknown parameters to be determined.

The reaction rates of methane with the change of partial pressure (the unit of partial pressure is atm.) of CH₄ and CO₂ are presented in Fig. 8. The corresponding kinetic parameters are shown in Table 4, of which the reaction orders, a and b, express the dependency relationship of reaction rate on partial pressure of components. Clearly, the partial pressure of both CH₄ and CO₂ have influence on the reaction rate. Compared with CO₂, partial pressure of methane has greater influence on the reaction kinetics, corresponding well with previous studies [47–50]. It should also be noted that the reaction order for Ni/CeO₂-SiO₂-P is lower than that of Ni/CeO₂-SiO₂-C, indicating less dependent reaction rates are affected by the partial pressure of reactants. CH₄ and CO₂ are both activated on the surface of catalyst on Ni/CeO₂-SiO₂-P.

According to Arrhenius equation $\ln k = -E_a/RT + C$, the slope of the linear relationship of $\ln k$ and $1/T$ is $-E_a/R$, where R is the gas constant. By this means the activation energies were calculated in DRM over the two catalysts in Fig. 8e and f. The values for Ni/CeO₂-SiO₂-P and Ni/CeO₂-SiO₂-C are 97.3 kJ/mol and 154.7 kJ/mol, respectively. The lower activation energy further confirms the higher reforming reactivity on Ni/CeO₂-SiO₂-P, which is in good consistent with the activity performance.

4.3. General investigation of the improved stability on Ni/CeO₂-SiO₂-P

Based on the results of characterization and catalytic performance, we propose the structure models of Ni/CeO₂-SiO₂-C and Ni/CeO₂-SiO₂-P and the long-term DRM reaction in Fig. 9. For Ni/CeO₂-SiO₂-C, CeO₂ locates away from Ni NPs with less reactive oxygen species on its surface (Fig. 9a). When CH₄ dissociates on the catalyst to active carbon species (C_a) and adsorbed H, the only conversion approach for C_a cannot efficiently and effectively reacts with reactive oxygen species to form CO, leading to the further accumulation and polymerization to less active C_b species and further to inactive C_y species, as evidenced by the formation of encapsulated carbon of Ni NPs in Fig. 6a. Ni/CeO₂-SiO₂-C quickly deactivates in the stability test as shown in Fig. 4. Although the presence of carbon filaments with Ni NPs on the top cause hardly the deactivation of the catalysts, the risk of reactor blockage increases with the prolonging of the reaction time. For Ni/CeO₂-SiO₂-P, the close interaction and contact of CeO₂ with Ni NPs render more reactive oxygen species and more interfacial sites (Fig. 9b). Ni NPs in close contact with

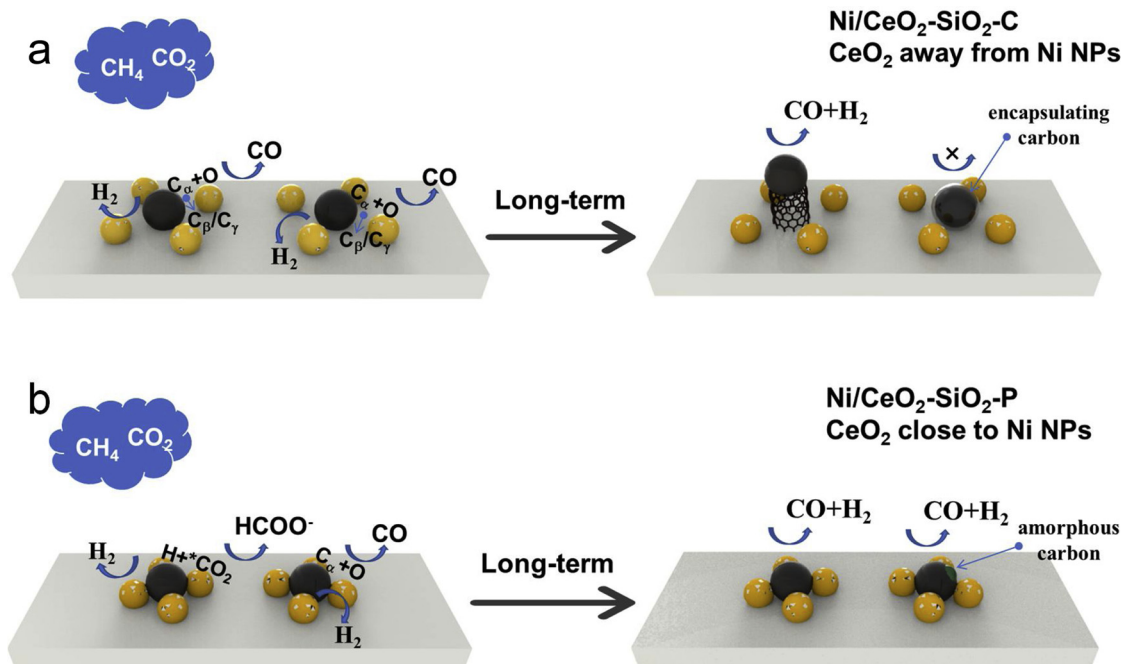


Fig. 9. Reaction pathways of dry reforming of CH₄ on (a) Ni/CeO₂-SiO₂-C and (b) Ni/CeO₂-SiO₂-P.

CeO_2 (more reactive oxygen species) are beneficial for the quick gasification of C_α species, preventing the growth or accumulation of inactive carbonaceous deposits. This route for elimination of C_α species on $\text{Ni}/\text{CeO}_2\text{-SiO}_2\text{-P}$ contributes to its stable catalytic performance in long-term reaction without the generation of inactive carbonaceous species. In addition, the appearance of formate species could also be beneficial to the enhanced catalytic performance.

5. Conclusions

In conclusion, $\text{Ni}/\text{CeO}_2\text{-SiO}_2\text{-C}$ and $\text{Ni}/\text{CeO}_2\text{-SiO}_2\text{-P}$ catalysts with similar Ni particle size and distribution are produced by the thermal-decomposed and plasma-decomposed approach. The main difference of the two catalysts is the interfacial structure between Ni and CeO_2 , which contains CeO_2 with more reactive oxygen species in close contact with Ni NPs on $\text{Ni}/\text{CeO}_2\text{-SiO}_2\text{-P}$ and CeO_2 with less reactive oxygen species away from Ni NPs on $\text{Ni}/\text{CeO}_2\text{-SiO}_2\text{-C}$. $\text{Ni}/\text{CeO}_2\text{-SiO}_2\text{-P}$ shows better catalytic performance for CO_2 and CH_4 conversions as well as high H_2/CO ratio in comparison with $\text{Ni}/\text{CeO}_2\text{-SiO}_2\text{-C}$ in the low temperature range ($\leq 700^\circ\text{C}$). The lower activation energy of $\text{Ni}/\text{CeO}_2\text{-SiO}_2\text{-P}$ than that of $\text{Ni}/\text{CeO}_2\text{-SiO}_2\text{-C}$ also confirms the higher reforming reactivity of the former based on the kinetic studies. Most significantly, $\text{Ni}/\text{CeO}_2\text{-SiO}_2\text{-P}$ is not only active but also stable with the ratio of H_2/CO at ~0.88 as well as CO_2 and CH_4 conversions at 88% and 78%, respectively at 700°C ; whereas $\text{Ni}/\text{CeO}_2\text{-SiO}_2\text{-C}$ has poor stability and loses its activity (CO conversion reducing from about 84% to 73% and CH_4 conversion declining from 71% to 58% with the ratio of H_2/CO decreasing from 0.87 to 0.83) within 15 h. The enhanced catalytic property and stability on $\text{Ni}/\text{CeO}_2\text{-SiO}_2\text{-P}$ originates from the unique interfacial structure, which facilitates the formation of formate species and the reaction of original and active C_α species via more available oxygen species and more accessible sites with hydrogen on the metal-support interface. The insufficient conversion of active C_α species via only reactive oxygen species on $\text{Ni}/\text{CeO}_2\text{-SiO}_2\text{-C}$ leads to the accumulation and polymerization to less active C_β species and further to inactive C_γ species, which deactivates the catalytic performance in short period of time. This work demonstrates that the metal-support interface can be designed and controlled for developing highly efficient and stable Ni-based catalysts.

Acknowledgements

The authors acknowledge the financial supports from the National Natural Science Foundation of China (No. 21878203), Shanxi International Cooperation Project (No. 201703D421037), Shanxi Provincial Key Innovative Research Team in Science and Technology (No. 2014131006), Natural Science Foundation of Shanxi Province (No. 201801D121061), Shanxi Province Science Foundation for Youths (No. 201601D202019), Program for the Outstanding Innovative Teams of Higher Learning Institutions of Shanxi (154010146-s), and Scientific and Technological Innovation Programs of Higher Education Institutions in Shanxi (No. 2017137).

Appendix A. Supplementary data

Supplementary material related to this article can be found, in the online version, at doi:<https://doi.org/10.1016/j.apcatb.2019.01.070>.

References

- [1] X. Tu, J.C. Whitehead, Plasma-catalytic dry reforming of methane in an atmospheric dielectric barrier discharge: understanding the synergistic effect at low temperature, *Appl. Catal. B: Environ.* 125 (2012) 439–448.
- [2] H.Q. Wang, X.L. Dong, T.T. Zhao, H.R. Yu, M. Li, Dry reforming of methane over bimetallic Ni-Co catalyst prepared from $\text{La}(\text{Co}_{1-x}\text{Ni}_x)_{0.5}\text{Fe}_{0.5}\text{O}_3$ perovskite precursor: catalytic activity and coking resistance, *Appl. Catal. B: Environ.* 245 (2019) 302–313.
- [3] I.V. Yentekakis, G. Goula, M. Hatzisymeon, I. Betsi-Arygropoulou, G. Botzolaki, K. Kousi, D.I. Kondarides, M.J. Taylor, C.M.A. Parlett, A. Osiatashiani, G. Kyriakou, J.P. Holgado, R.M. Lambert, Effect of support oxygen storage capacity on the catalytic performance of Rh nanoparticles for CO_2 reforming of methane, *Appl. Catal. B: Environ.* 243 (2019) 490–501.
- [4] S.C. Rood, H.B. Ahmet, A. Gomez-Ramon, L. Torrente-Murciano, T.R. Reina, S. Eslava, Enhanced ceria nanoflakes using graphene oxide as a sacrificial template for CO oxidation and dry reforming of methane, *Appl. Catal. B: Environ.* 242 (2019) 358–368.
- [5] E. le Saché, L. Pastor-Pérez, D. Watson, A. Sepúlveda-Escribano, T.R. Reina, Ni stabilised on inorganic complex structures: superior catalysts for chemical CO_2 recycling via dry reforming of methane, *Appl. Catal. B: Environ.* 236 (2018) 458–465.
- [6] S.P. Wen, M.L. Liang, J.M. Zou, S. Wang, X.D. Zhu, L. Liu, Z.J. Wang, Synthesis of a SiO_2 nanofibre confined Ni catalyst by electrospinning for the CO_2 reforming of methane, *J. Mater. Chem. A* 3 (2015) 13299–13307.
- [7] X.H. Zhang, L. Zhang, H.G. Peng, X.J. You, C. Peng, X.L. Xu, W.M. Liu, X.Z. Fang, Z. Wang, N. Zhang, X. Wang, Nickel nanoparticles embedded in mesopores of AlSBA-15 with a perfect peacock-like structure: a catalyst with superior sintering resistance and hydrothermal stability for methane dry reforming, *Appl. Catal. B: Environ.* 224 (2018) 488–499.
- [8] M. Zhang, J.F. Zhang, Y.Q. Wu, J.X. Pan, Q.D. Zhang, Y.S. Tan, Y.Z. Han, Insight into the effects of the oxygen species over Ni/ZrO_2 catalyst surface on methane reforming with carbon dioxide, *Appl. Catal. B: Environ.* 244 (2019) 427–437.
- [9] L.L. Xu, H.L. Song, L.J. Chou, Carbon dioxide reforming of methane over ordered mesoporous $\text{NiO}\text{-MgO}\text{-Al}_2\text{O}_3$ composite oxides, *Appl. Catal. B: Environ.* 108–109 (2011) 177–190.
- [10] S.R. Li, J.L. Gong, Strategies for improving the performance and stability of Ni-based catalysts for reforming reactions, *Chem. Soc. Rev.* 43 (2014) 7245–7256.
- [11] M. Shirazi, E.C. Neyts, A. Bogaerts, DFT study of Ni-catalyzed plasma dry reforming of methane, *Appl. Catal. B: Environ.* 205 (2017) 605–614.
- [12] C.J. Liu, J.Y. Ye, J.Y. Jiang, Y.X. Pan, Progresses in the preparation of coke resistant Ni-based catalyst for steam and CO_2 reforming of methane, *ChemCatChem* 3 (2011) 529–541.
- [13] J.S. Zhang, F.X. Li, Coke-resistant Ni/SiO_2 catalyst for dry reforming of methane, *Appl. Catal. B: Environ.* 176–177 (2015) 513–521.
- [14] X.L. Zhu, P.P. Huo, Y.P. Zhang, D.G. Cheng, C.J. Liu, Structure and reactivity of plasma treated $\text{Ni}/\text{Al}_2\text{O}_3$ catalyst for CO_2 reforming of methane, *Appl. Catal. B: Environ.* 81 (2008) 132–140.
- [15] J.W. Han, J.S. Park, M.S. Choi, H. Lee, Uncoupling the size and support effects of Ni catalysts for dry reforming of methane, *Appl. Catal. B: Environ.* 203 (2017) 625–632.
- [16] T. Margossian, K. Larmier, S.M. Kim, F. Krumeich, A. Fedorov, P. Chen, C.R. Müller, C. Copéret, Molecularly tailored nickel precursor and support yield a stable methane dry reforming catalyst with superior metal utilization, *J. Am. Chem. Soc.* 139 (2017) 6919–6927.
- [17] A. Nandini, K.K. Pant, S.C. Dhingra, K., CeO_2 , and Mn-promoted $\text{Ni}/\text{Al}_2\text{O}_3$ catalysts for stable CO_2 reforming of methane, *Appl. Catal. A Gen.* 290 (2005) 166–174.
- [18] H. Tian, X.Y. Li, L. Zeng, J.L. Gong, Recent advances on the design of group VIII base-metal catalysts with encapsulated structures, *ACS Catal.* 5 (2015) 4959–4977.
- [19] M. Steib, Y. Lou, A. Jentys, J.A. Lercher, Enhanced activity in methane dry reforming by carbon dioxide induced metal-oxide interface restructuring of nickel/zirconia, *ChemCatChem* 9 (2017) 3809–3813.
- [20] M. Shah, S. Das, A.K. Nayak, P. Mondal, A. Bordoloi, Smart designing of metal-support interface for imperishable dry reforming catalyst, *Appl. Catal. A Gen.* 556 (2018) 137–154.
- [21] L. Foppa, T. Margossian, S.M. Kim, C. Müller, C. Copéret, K. Larmier, A. Comas-Vives, Contrasting the role of $\text{Ni}/\text{Al}_2\text{O}_3$ interfaces in water-gas shift and dry reforming of methane, *J. Am. Chem. Soc.* 139 (2017) 17128–17139.
- [22] V.M. Gonzalez-DelaCruz, J.P. Holgado, R. Pereñíguez, A. Caballero, Morphology changes induced by strong metal-support interaction on a Ni-ceria catalytic system, *J. Catal.* 257 (2008) 307–314.
- [23] Y. Lu, D. Guo, Y.Z. Ruan, Y.J. Zhao, S.P. Wang, X.B. Ma, Facile one-pot synthesis of Ni@HSS as a novel yolk-shell structure catalyst for dry reforming of methane, *J. CO₂ Util.* 24 (2018) 190–199.
- [24] T. Odedairo, J.L. Chen, Z.H. Zhu, Metal-support interface of a novel Ni-CeO_2 catalyst for dry reforming of methane, *Catal. Commun.* 31 (2013) 25–31.
- [25] Z.Y. Liu, D.C. Grinter, P.G. Lustemberg, T.D. Nguyen-Phan, Y.H. Zhou, S. Luo, I. Waluyo, E.J. Crumlin, D. Stacchiola, J. Zhou, J. Carrasco, H.F. Busnengo, M.V. Ganduglia-Pirovano, S.D. Senanayake, J.A. Rodriguez, Dry reforming of methane on a highly-active Ni-CeO_2 catalyst: effects of metal-support interactions on C-H bond breaking, *Angew. Chem. Int. Ed.* 55 (2016) 7455–7459.
- [26] J.B. Wang, Y.L. Tai, W.P. Dow, T.J. Huang, Study of ceria-supported nickel catalyst and effect of yttria doping on carbon dioxide reforming of methane, *Appl. Catal. A Gen.* 218 (2001) 69–79.
- [27] X.L. Yan, B.R. Zhao, Y. Liu, Y.N. Li, Dielectric barrier discharge plasma for preparation of Ni-based catalysts with enhanced coke resistance: current status and perspective, *Catal. Today* 256 (2015) 29–40.
- [28] X.L. Yan, Y. Liu, B.R. Zhao, Z. Wang, Y. Wang, C.J. Liu, Methanation over Ni/SiO_2 : effect of the catalyst preparation methodologies, *Int. J. Hydrogen Energy* 38 (2013) 2283–2291.
- [29] G. Pantaleo, V. La Parola, F. Deganello, R.K. Singha, R. Bal, A.M. Venezia, Ni/CeO_2 catalysts for methane partial oxidation: synthesis driven structural and catalytic effects, *Appl. Catal. B: Environ.* 189 (2016) 233–241.
- [30] G. Pantaleo, V. La Parola, F. Deganello, P. Calatocco, Rajaram Bal, A.M. Venezia, Synthesis and support composition effects on CH_4 partial oxidation over Ni-CeLa oxides, *Appl. Catal. B: Environ.* 164 (2015) 135–143.

- [31] D. Alders, F.C. Voogt, T. Hibma, G.A. Sawatzky, Nonlocal screening effects in 2p x-ray photoemission spectroscopy of NiO (100), *Phys. Rev. B* 54 (1996) 7716–7719.
- [32] E.T. Saw, U. Oemar, X.R. Tan, Y. Du, A. Borgna, K. Hidajat, S. Kawi, Bimetallic Ni–Cu catalyst supported on CeO₂ for high-temperature water–gas shift reaction: methane suppression via enhanced CO adsorption, *J. Catal.* 314 (2014) 32–46.
- [33] A. Vito, C. Italiano, L. Pino, P. Frontera, M. Ferraro, V. Antonucci, Activity and stability of powder and monolith-coated Ni/GDC catalysts for CO₂ methanation, *Appl. Catal. B: Environ.* 226 (2018) 384–395.
- [34] M.J. Yu, Y.A. Zhu, Y. Lu, G.S. Tong, K.K. Zhu, X.G. Zhou, The promoting role of Ag in Ni-CeO₂ catalyzed CH₄-CO₂ dry reforming reaction, *Appl. Catal. B: Environ.* 165 (2015) 43–56.
- [35] X.P. Duan, Z.J. Wen, Y.X. Zhao, J.F. Zhou, H.H. Fang, Y.N. Cao, L.L. Jiang, L.M. Ye, Y.Z. Yuan, Intercalation of nanostructured CeO₂ in MgAl₂O₄ spinel illustrates the critical interaction between metal oxides and oxides, *Nanoscale* 10 (2018) 3331–3341.
- [36] M. Machida, M. Uto, D. Kurogi, T. Kijima, MnO_x–CeO₂ binary oxides for catalytic NO_x sorption at low temperatures. Sorptive removal of NO_x, *Chem. Mater.* 12 (2000) 3158–3164.
- [37] Z. Zhang, X. Verykios, Carbon dioxide reforming of methane to synthesis gas over supported Ni catalysts, *Catal. Today* 21 (1994) 589–595.
- [38] D.W. Goodwan, R.D. Kelley, T.E. Maday, J.M. White, Measurement of carbide buildup and removal kinetics on Ni (100), *J. Catal.* 64 (1980) 479–481.
- [39] X.Y. Quek, D.P. Liu, W.N.E. Cheo, H. Wang, Y. Chen, Y.H. Yang, Nickel-grafted TUD-1 mesoporous catalysts for carbon dioxide reforming of methane, *Appl. Catal. B: Environ.* 95 (2010) 374–382.
- [40] B.R. Zhao, X.L. Yan, Y. Zhou, C.J. Liu, Effect of catalyst structure on growth and reactivity of carbon nanofibers over Ni/MgAl₂O₄, *Ind. Eng. Chem. Res.* (2013) 8182–8188.
- [41] D. Gamarra, A. Martínez-Arias, Preferential oxidation of CO in rich H₂ over CuO/CeO₂: operando-DRIFTS analysis of deactivating effect of CO₂ and H₂O, *J. Catal.* 263 (2009) 189–195.
- [42] S. Li, Q.Q. Wang, X.L. Yan, H.Q. Zhuang, C. Yuan, J.P. Feng, M.J. Wang, R.F. Li, W.Y. Li, Y.X. Pan, Al₂O₃ support triggering highly efficient photoreduction of CO₂ with H₂O on noble-metal-free CdS/Ni₉S₈/Al₂O₃, *Appl. Catal. B: Environ.* 240 (2019) 174–181.
- [43] M.M. Schubert, H.A. Gasteiger, R.J. Behm, Surface formates as side products in the selective CO oxidation on Pt/γ-Al₂O₃, *J. Catal.* 172 (1997) 256–258.
- [44] D. Pakhare, J. Spivey, A review of dry (CO₂) reforming of methane over noble metal catalysts, *Chem. Soc. Rev.* 43 (2014) 7813–7837.
- [45] P. Ferreira-Aparicio, M. Fernandez-Garcia, A. Guerrero-Ruiz, I. Rodriíguez-Ramos, Evaluation of the role of the metal-support interfacial centers in the dry reforming of methane on alumina-supported rhodium catalysts, *J. Catal.* 190 (2000) 296–308.
- [46] J.Z. Luo, Z.L. Yu, C.F. Ng, C.T. Au, CO₂/CH₄ Reforming over Ni-La₂O₃/5A: an investigation on carbon deposition and reaction steps, *J. Catal.* 194 (2000) 198–210.
- [47] N. Laosiripojana, W. Suthisripok, S. Assabumrungrat, Synthesis gas production from dry reforming of methane over CeO₂ doped Ni/Al₂O₃: influence of the doping ceria on the resistance toward carbon formation, *Chem. Eng. J.* 112 (2005) 13–22.
- [48] R.K. Singha, A. Yadav, A. Agrawal, A. Shukla, S. Adak, T. Sasaki, R. Bal, Synthesis of highly coke resistant Ni nanoparticles supported MgO/ZnO catalyst for reforming of methane with carbon dioxide, *Appl. Catal. B: Environ.* 191 (2016) 165–178.
- [49] D. Pakhare, V. Schwartz, V. Abdelsayed, D. Haynes, D. Shekhawat, J. Poston, J. Spivey, Kinetic and mechanistic study of dry (CO₂) reforming of methane over Rh-substituted La₂Zr₂O₇ pyrochlores, *J. Catal.* 316 (2014) 78–92.
- [50] S. Das, S. Thakur, A. Bag, M.S. Gupta, P. Mondal, A. Bordoloi, Support interaction of Ni nanocluster based catalysts applied in CO₂ reforming, *J. Catal.* 330 (2015) 46–60.